

## Dominant $\beta$ -catenin mutations cause intellectual disability with recognizable syndromic features

Valter Tucci, ... , Sara Wells, Patrick M. Nolan

*J Clin Invest.* 2014;**124**(4):1468-1482. <https://doi.org/10.1172/JCI70372>.

Research Article

Neuroscience

The recent identification of multiple dominant mutations in the gene encoding  $\beta$ -catenin in both humans and mice has enabled exploration of the molecular and cellular basis of  $\beta$ -catenin function in cognitive impairment. In humans,  $\beta$ -catenin mutations that cause a spectrum of neurodevelopmental disorders have been identified. We identified de novo  $\beta$ -catenin mutations in patients with intellectual disability, carefully characterized their phenotypes, and were able to define a recognizable intellectual disability syndrome. In parallel, characterization of a chemically mutagenized mouse line that displays features similar to those of human patients with  $\beta$ -catenin mutations enabled us to investigate the consequences of  $\beta$ -catenin dysfunction through development and into adulthood. The mouse mutant, designated batface (*Bfc*), carries a Thr653Lys substitution in the C-terminal armadillo repeat of  $\beta$ -catenin and displayed a reduced affinity for membrane-associated cadherins. In association with this decreased cadherin interaction, we found that the mutation results in decreased intrahemispheric connections, with deficits in dendritic branching, long-term potentiation, and cognitive function. Our study provides in vivo evidence that dominant mutations in  $\beta$ -catenin underlie losses in its adhesion-related functions, which leads to severe consequences, including intellectual disability, childhood hypotonia, progressive spasticity of lower limbs, and abnormal craniofacial features in adults.

Find the latest version:

<https://jci.me/70372/pdf>





# Dominant $\beta$ -catenin mutations cause intellectual disability with recognizable syndromic features

Valter Tucci,<sup>1,2</sup> Tjitske Kleefstra,<sup>3</sup> Andrea Hardy,<sup>2</sup> Ines Heise,<sup>2</sup> Silvia Maggi,<sup>1</sup> Marjolein H. Willemsen,<sup>3</sup> Helen Hilton,<sup>2</sup> Chris Esapa,<sup>2</sup> Michelle Simon,<sup>2</sup> Maria-Teresa Buenavista,<sup>4,5</sup> Liam J. McGuffin,<sup>4</sup> Lucie Vizor,<sup>2</sup> Luca Doderò,<sup>6</sup> Sotirios Tsaftaris,<sup>6,7</sup> Rosario Romero,<sup>2</sup> Willy N. Nillesen,<sup>3</sup> Lisenka E.L.M. Vissers,<sup>3</sup> Marlies J. Kempers,<sup>3</sup> Anneke T. Vulto-van Silfhout,<sup>3</sup> Zafar Iqbal,<sup>3</sup> Marta Orlando,<sup>1</sup> Alessandro Maccione,<sup>1</sup> Glenda Lassi,<sup>1</sup> Pasqualina Farisello,<sup>1</sup> Andrea Contestabile,<sup>1</sup> Federico Tinarelli,<sup>1</sup> Thierry Nieuw,<sup>1</sup> Andrea Raimondi,<sup>1</sup> Barbara Greco,<sup>1</sup> Daniela Cantatore,<sup>1</sup> Laura Gasparini,<sup>1</sup> Luca Berdondini,<sup>1</sup> Angelo Bifone,<sup>6</sup> Alessandro Gozzi,<sup>6</sup> Sara Wells,<sup>2</sup> and Patrick M. Nolan<sup>2</sup>

<sup>1</sup>Department of Neuroscience and Brain Technologies, Istituto Italiano di Tecnologia, Genova, Italy. <sup>2</sup>MRC Harwell, Harwell Science and Innovation Campus, Oxfordshire, United Kingdom. <sup>3</sup>Department of Human Genetics, Radboud University Medical Center, Nijmegen, Netherlands.

<sup>4</sup>School of Biological Sciences, University of Reading, Reading, United Kingdom. <sup>5</sup>Beamline B23, Diamond Light Source, Didcot, Oxford, United Kingdom.

<sup>6</sup>Istituto Italiano di Tecnologia Center for Neuroscience and Cognitive Systems, Rovereto, Italy. <sup>7</sup>IMT Institute for Advanced Studies Lucca, Lucca, Italy.

**The recent identification of multiple dominant mutations in the gene encoding  $\beta$ -catenin in both humans and mice has enabled exploration of the molecular and cellular basis of  $\beta$ -catenin function in cognitive impairment. In humans,  $\beta$ -catenin mutations that cause a spectrum of neurodevelopmental disorders have been identified. We identified de novo  $\beta$ -catenin mutations in patients with intellectual disability, carefully characterized their phenotypes, and were able to define a recognizable intellectual disability syndrome. In parallel, characterization of a chemically mutagenized mouse line that displays features similar to those of human patients with  $\beta$ -catenin mutations enabled us to investigate the consequences of  $\beta$ -catenin dysfunction through development and into adulthood. The mouse mutant, designated batface (*Bfc*), carries a Thr653Lys substitution in the C-terminal armadillo repeat of  $\beta$ -catenin and displayed a reduced affinity for membrane-associated cadherins. In association with this decreased cadherin interaction, we found that the mutation results in decreased intrahemispheric connections, with deficits in dendritic branching, long-term potentiation, and cognitive function. Our study provides in vivo evidence that dominant mutations in  $\beta$ -catenin underlie losses in its adhesion-related functions, which leads to severe consequences, including intellectual disability, childhood hypotonia, progressive spasticity of lower limbs, and abnormal craniofacial features in adults.**

## Introduction

$\beta$ -Catenin (CTNNB1) is a highly conserved protein that implements key cellular functions by interacting with cell-adhesion proteins, signaling molecules, and transcription factors (1). The characteristic structural feature of the  $\beta$ -catenin protein, its 12 central armadillo repeats, forms a long positively charged groove facilitating interaction with multiple protein partners. This central motif is flanked by the N terminus, crucial in mediating degradation of the protein, and the C terminus, containing the Helix-C motif (2), which enables switching between the protein's dual roles in cell adhesion and proliferation. Loss-of-function studies in mammals have implicated  $\beta$ -catenin in embryonic development, while gain-of-function studies have demonstrated its contribution to various forms of human cancers (reviewed in ref. 3). Functional investigation has focused on the role of  $\beta$ -catenin in canonical WNT signaling.  $\beta$ -Catenin interacts with transcriptional coactivators to mediate WNT's transcriptional activation, which orchestrates growth and patterning in the developing embryo, and, when constitutively upregulated, dysregulates growth connected to cancer and metastasis.

In addition to its role in the WNT-signaling pathway,  $\beta$ -catenin serves as a major intracellular anchor for membrane cadherins, a family of cell-adhesion molecules that modulate synaptic connectivity (4). The intracellular domains of cadherins can establish interactions across the whole central 12-armadillo motifs of  $\beta$ -catenin. This interaction integrates multiple, independent processes (5), such as maintaining cell adhesion and regulating cell migration and neurite outgrowth (6, 7). One model proposes that  $\beta$ -catenin participates in synaptic remodeling through regulating these interactions (8). Because synaptic changes are key cellular processes underlying memory (9), regulated stability of the cadherin-catenin complex could be a cellular mediator of memory. In fact, using a conditional null mutant,  $\beta$ -catenin has been shown to play a significant role in long-term memory consolidation (10).

Through high-throughput genomics approaches, evidence implicating  $\beta$ -catenin in human cognitive disorders has come to light recently (11, 12). Large-scale sequencing efforts have found that rare de novo point mutations in *CTNNB1* represent a major contribution to intellectual disability (ID) (13) and to autism spectrum disorders (ASD) (12). These studies have uncovered 4 potential causative mutations in *CTNNB1*; 3 were loss-of-function mutations in patients with ID (p.Ser425Thrfs\*11, p.Arg515\* and p.Gln309\*) (13) and one was a missense mutation in a patient with ASD

**Conflict of interest:** The authors have declared that no conflict of interest exists.

**Citation for this article:** *J Clin Invest.* 2014;124(4):1468–1482. doi:10.1172/JCI70372.





features associated with human de novo  $\beta$ -catenin mutations. We performed detailed phenotype studies in the 4 individuals with ID and concluded that they displayed highly similar and specific features that led us to define what we believe to be a novel recognizable syndrome comprising mild to severe ID, ASD childhood hypotonia with progressive spastic diplegia, (primary) microcephaly, and significant additional craniofacial and brain abnormalities, including corpus callosum hypoplasia (Figure 1A). Additional clinical descriptions are included in the Supplemental Clinical Description (supplemental material available online with this article; doi:10.1172/JCI70372DS1). As all ID mutations identified (Figure 1F) predict loss-of-function, resulting in significant protein truncation, we investigated whether the mutant mRNAs would undergo nonsense-mediated decay. This was observed in 2 of the 4 individuals using allele-specific cDNA amplification of EBV-treated patient lymphocytes in the presence or absence of cycloheximide (Supplemental Figure 1). These results suggested that *CTNNB1* haploinsufficiency is responsible for the craniofacial and ID phenotypes in the patients.

*An ENU mutagenesis screen reveals a  $\beta$ -catenin mouse mutant.* In a parallel study, we identified a single animal within a G1 population of ENU-mutagenized animals (14) showing a dominant craniofacial phenotype with characteristic broad facial features (Figure 1, B and C). Named batface (*Bfc*, MGI:2656734) because of its distinct craniofacial dysmorphology, the phenotype was inherited in a dominant fashion while intercrosses revealed that the mutation was homozygous lethal with lethality occurring at mid to late gestation (15). We mapped the dominant craniofacial phenotype at low resolution using 13 affected animals. Finding a single region of linkage on distal chromosome 9, we used additional markers and animals and refined the nonrecombinant region to 0.56 Mb between 120.92 Mb and 121.48 Mb. As only 2 transcripts mapped to the region, we sequenced all coding exons and identified a single missense mutation, a C-to-A transition, in exon 13 of the  $\beta$ -catenin gene (*Ctnnb1*; Figure 1D). The mutation results in a Thr653Lys substitution in the highly conserved 12th armadillo repeat at the C-terminal end of the protein (Figure 1E). Initial functional investigations in midgestational embryos suggested that the *Bfc* mutation acts through a gain-of-function in the WNT-mediated transcriptional pathway (15). However, unlike other gain- or loss-of-function mutations in  $\beta$ -catenin, this was the first example of a mouse mutation, to our knowledge, to reference a craniofacial dysmorphology in heterozygous adults. Significant cranial differences occur in *Ctnnb1<sup>Bfc/+</sup>* (*Bfc/+*) mice compared with littermate controls, including a shortened nasal length and an augmentation of the interorbital distance and of the bregma to bony ridge length (Figure 1C and Supplemental Figure 2). In considering the similar overt features of *CTNNB1* mutations in humans and *Bfc/+* mice, we were prompted to assess the nature of the *Bfc* mutation in mice. So we carried out a number of protein function studies to investigate whether any of the prominent roles of *CTNNB1* could be compromised in *Bfc/+* mice.

*The *Bfc* mutation disrupts the cadherin- $\beta$ -catenin interaction.* To determine the nature of the *Bfc* mutation, we first examined whether protein levels were affected (Supplemental Figure 3). As no differences were identified in Western blots, we investigated whether the mutation could affect the ability of  $\beta$ -catenin to interact with any of its known interacting partners. Specifically, the role of the C-terminal armadillo repeat has been well documented in anchoring membrane-bound cadherins to the intracellular cytoskeleton (5, 16). Moreover, the tyrosine residue adjacent to the *Bfc* mutation (Tyr654) is crucial in maintaining this interaction. Docking of an N-terminal  $\alpha$ -helix

in cadherin within a groove formed by armadillo repeats 11 to 12 of  $\beta$ -catenin can be reduced by 85% when Tyr654 is phosphorylated (17). To investigate whether Thr653Lys would similarly disrupt the docking of the N-terminal cadherin helix, we immunoprecipitated native protein from WT and *Bfc/+* adult hippocampal whole-cell lysates. Strikingly, we found that the cadherin-catenin interaction was significantly reduced, by 46% ( $P < 0.01$ ;  $t$  test) in *Bfc/+* hippocampus (Figure 2, A and B). This reduced affinity of mutant  $\beta$ -catenin for cadherin was subsequently confirmed in immunoprecipitates from HEK293 cells transiently transfected with N-cadherin and  $\beta$ -catenin mammalian expression constructs (Figure 2, C and D). Using available models of  $\beta$ -catenin and E-cadherin structure, we investigated whether a Thr653Lys substitution had the potential to disrupt interactions between these 2 proteins (Figure 2, E–H, and Supplemental Figure 4). From the superposition of the 3D models of mutant, WT, and Tyr654-p  $\beta$ -catenin (Figure 2H), Tyr654-p has been observed to break the hydrogen bond with Asp665 in cadherin (5). In investigating the interacting helices of  $\beta$ -catenin and cadherin, it would appear that the predicted 3D model of mutant  $\beta$ -catenin shows a disruption of the interaction with cadherin, causing a steric bulge, similar in effect to the Tyr654-p.

*Morphological analysis reveals brain abnormalities in *Bfc/+* mice.* We proceeded to characterize *Bfc* at neuroanatomical and behavioral levels. Using MRI, we found a number of major abnormalities in mutants. The anteroposterior axis was significantly shortened, whereas the dorsoventral and medial-lateral axes were enlarged (Figure 3, A and B). In contrast to what was found in mice overexpressing  $\beta$ -catenin (18), gyrification of the cerebral cortex was not observed. However, gray matter and total brain volumes were significantly larger in *Bfc/+* ( $P < 0.05$ ; 1-way ANOVA, Supplemental Figure 5A). When normalized to brain volume, however, the relative gray matter and white matter content in *Bfc/+* was not statistically different from that of controls (Supplemental Figure 5B). Alterations in the absolute and relative volume of multiple anatomical brain structures were also found (Supplemental Figure 6). The thalamus, striatum, and globus pallidus were slightly, but significantly, larger in *Bfc/+*. However, mutants showed substantially reduced cerebellar and olfactory bulb volumes compared with WT. In addition to these general morphological features, the corpus callosum appeared to be severely underdeveloped in 3 *Bfc/+* individuals, lacking any interhemispheric extensions (Figure 3, C–E). This was reminiscent of the human case with callosal hypoplasia described above. No evidence of major corpus callosum alterations was observed in the remaining *Bfc/+* brains or in the control group. Reductions in olfactory bulb, cerebellum size, and abnormal corpus callosum found with MRI were confirmed in histopathological sections of mouse brain (Supplemental Figure 7).

**Bfc* mutant mice show deficits in sensorimotor gating, motor function, and vocalization complexity.* We studied specific behaviors in mice that related to deficits evident in the human ID cases, including motor dysfunction, cognitive disabilities, and vocalization deficiencies. Acoustic startle response (ASR) (Figure 4A) and prepulse inhibition (PPI) (Figure 4B) of ASR reflect the ability of an animal to respond to and integrate sensory information (19). *Bfc/+* mice showed consistent and significant PPI deficits, whereas ASR was normal. Motor deficits were present but were more subtle. On a typical rotarod test, *Bfc/+* mice showed no significant deficit (data not shown). However, when tested with a more challenging test incorporating 6 consecutive accelerating stages in a single session, *Bfc/+* mice showed a significantly shorter latency period before falling from the rod, and these differences were maintained when trials were

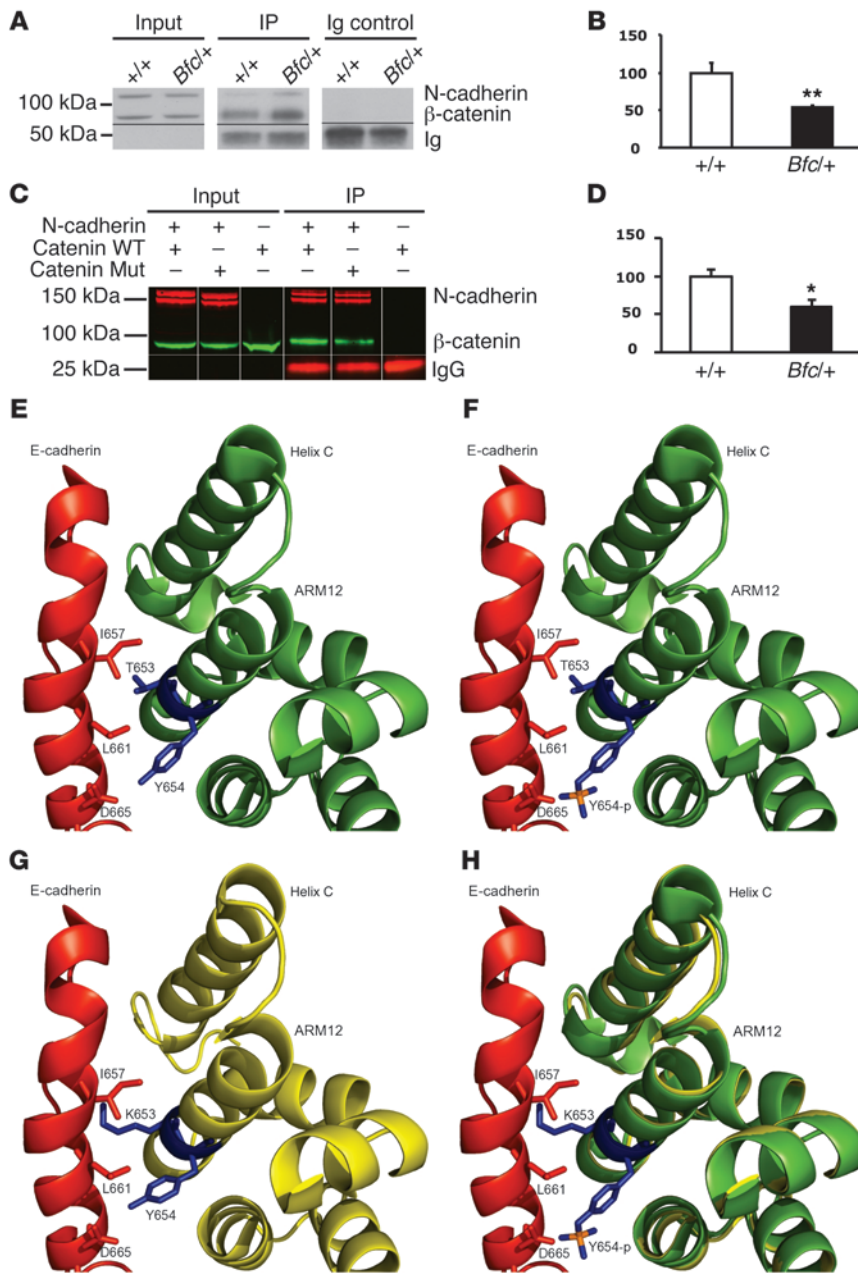


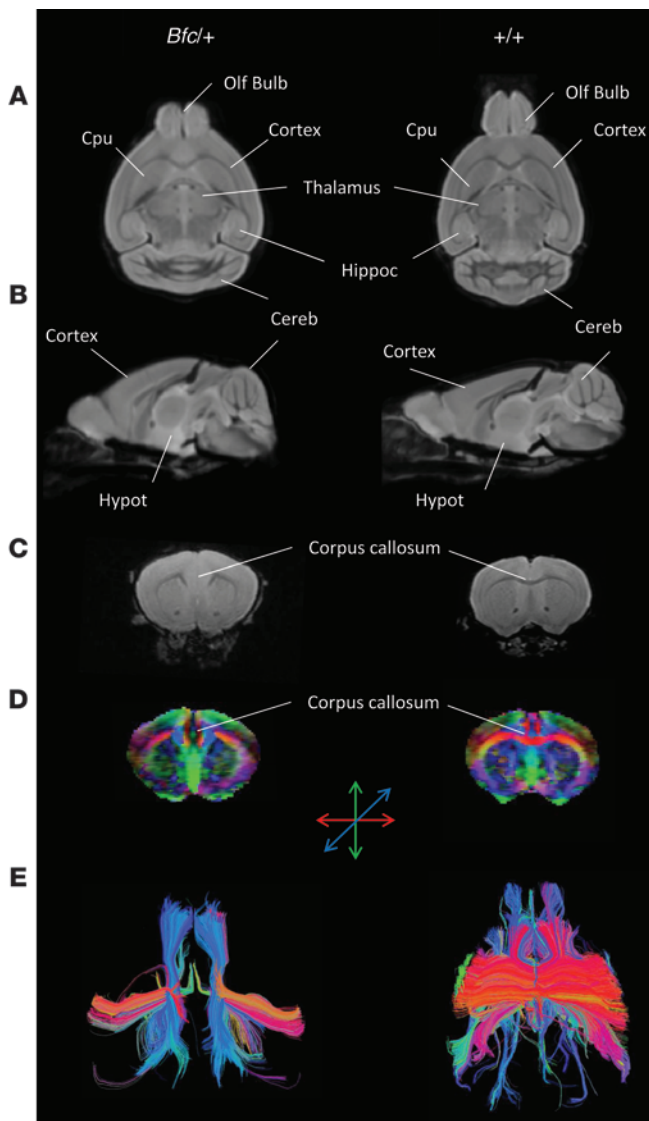
**Figure 2**

The Thr653Lys mutation disrupts the murine β-catenin–cadherin complex. **(A)** Western blot of adult hippocampal whole-cell lysates immunoprecipitated with anti-N-cadherin. Typical N-cadherin and β-catenin immunoreactive bands are shown. An Ig control lysate IP using normal rabbit IgG is included. Black lines indicate noncontiguous regions. **(B)** β-catenin immunoreactivity was normalized to immunoprecipitated N-cadherin, revealing a 46% reduced interaction in mutant hippocampal lysates ( $n = 7$ ,  $**P < 0.01$ ). **(C)** Western blot of lysates from HEK293 cells transfected with N-cadherin–EGFP and β-catenin–V5/His and immunoprecipitated with anti-EGFP. Control IPs were carried out from cells transfected with only the WT β-catenin–V5/His plasmid. White lines indicate noncontiguous regions. **(D)** Recombinant β-catenin immunoreactivity was normalized to immunoprecipitated recombinant N-cadherin, confirming reduced interaction (40% reduction,  $n = 3$ ,  $*P = 0.03$ ). **(E)** Close-up view of the interacting residues in the WT complex. β-catenin is shown in green. T653 and Y654 (blue sticks) in β-catenin are both located on the surface of the ARM12 helix 3. E-cadherin (red) helix is shown with contacting residues D665 and L661. D665 of E-cadherin forms the hydrogen bond with Y654. **(F)** Description is the same as in **E**; however, the phosphorylated tyrosine (Y654-p) residue is shown. **(G)** Close-up view of interacting residues in the mutant form (T653K). K653 (blue sticks) is shown in the IntFOLD2 (35, 36) model of the β-catenin armadillo domain (yellow). The mutant residue extends to contact the E-cadherin backbone (red). **(H)** 3D-modeled β-catenin with the K653 mutation superimposed on the crystal structure of β-catenin, showing K653 with Y654-p vis-a-vis the E-cadherin-interacting residues: D665, L661, and I657.

repeated over 3 days (Figure 4C). Mice emit ultrasonic vocalizations under certain conditions, such as maternal separation. We tested ultrasonic vocalizations at postnatal day 6 by separating pups from their mothers for 5 minutes. We observed a significant reduction in the total number of vocalizations in mutants (Figure 4D). The mean duration of each vocalization was slightly shorter, although not significant. Finally, mutant pups produced more calls characterized by a single component (Figure 4, E and F), suggesting that they have developed a less complex vocalization system.

**Learning and memory deficits in *Bfcl* mutants.** One of the defining characteristics of individuals with ID is the cognitive deficit. To investigate cognitive abilities in *Bfcl*+/+ mice, we used 2 hippocampus-related tests, the water maze (WM) test (20) and the fear conditioning test (21). In the WM, a test for spatial learning, we trained mice for 4 days

with a visible platform to trigger hippocampus-independent navigation followed by training with a hidden platform to measure hippocampus-dependent learning. We observed no differences in the latency period before finding the visible platform. However, while control animals improved their performance with the hidden platform, *Bfcl*+/+ mice did not improve (Figure 5A). *Bfcl*+/+ mice showed a consistent delay at probe trials at the end of each daily session (Figure 5B), although their swimming ability was normal (Figure 5, C and D), confirming a deficit in hippocampus-dependent performance. When *Bfcl*+/+ mice were tested in a standard fear conditioning protocol for contextual memory, their freezing behavior during reexposure to the context was significantly lower than that of littermate controls (Figure 5C), indicating that mutants have a reduced capacity to recall the previous shock exposure.

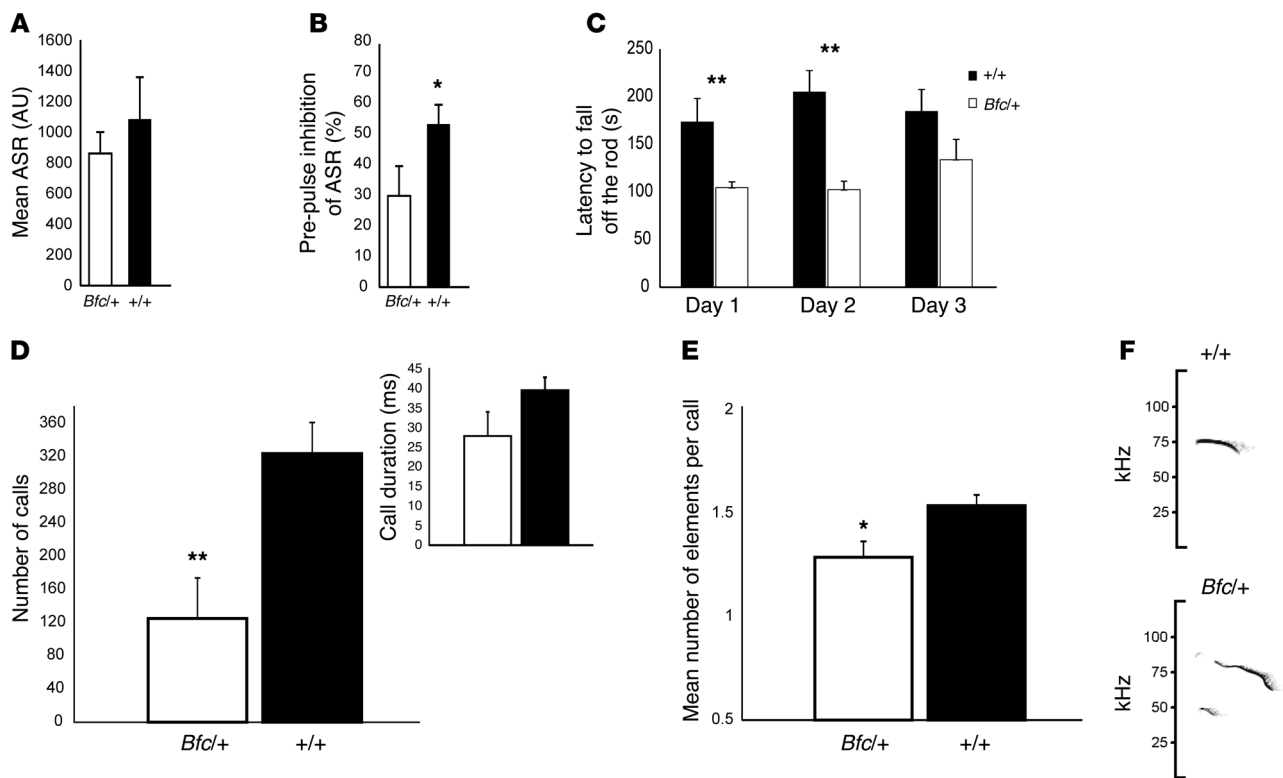
**Figure 3**

MRI scans of *Bfc/+* mice reveal major brain abnormalities. MRI scans of *Bfc/+* mice highlighted an altered cranial shape with a larger left-right axis and a shorter longitudinal extension compared with controls. The effect was apparent in horizontal (A) and sagittal (B) views of the brain. The olfactory bulbs and cerebellum appeared to be significantly smaller in *Bfc/+* individuals compared with control littermates. In 3 out of 10 *Bfc/+* subjects, the corpus callosum appeared to be severely underdeveloped, lacking any interhemispheric extension. This was apparent in anatomical T2-weighted images (C) as well as in diffusion-weighted scans (D and E). Diffusion tensor images (DTI) modulated by FA (D) and DTI tractography corroborated the lack of interhemispheric connection of the corpus callosum in all of the 3 subjects, showing abnormal callosal anatomy in anatomical MRI images (C, D, and E show data from representative *Bfc/+* and control subjects). Normal interhemispheric tracts were observed in all the control subject images. Cereb, cerebellum; Cpu, caudate putamen; Olf Bulb, olfactory bulbs; Hippoc, hippocampus; Hypot, hypothalamus.

times, indicating a lack of temporal coordination and perseverative behavior (Figure 6E). Furthermore, we tested whether mice were able to discriminate short- versus long-interval light signals by nose poking in the appropriate location. This test (24) assesses whether the animal has an accurate endogenous (subjective estimation of the signal duration) and exogenous (ratio between short and long signals) timing representation. Accuracy and precision were significantly worse in *Bfc/+* mice (Supplemental Figure 9, A and B) during the dark phase of the 12-hour light/12-hour-dark cycle, when mice are most active. This was confirmed by analysis of error rates (i.e., nose pokes in the inappropriate location). While the error rate in control mice increased only during the light phase, *Bfc/+* mice had a constant high error rate (Figure 6, F and G).

*Synaptic morphology and functionality are altered in Bfc mice.* We investigated whether behavioral deficits might be associated with deficits in neuronal architecture and functional connectivity in *Bfc/+* brains. We first looked at neurite growth and arborization in primary neurons cultured from embryonic hippocampus. We found that the morphology of both heterozygous and homozygous *Bfc* neurons was different after only 1 day in culture (Supplemental Figure 10A). In particular, the length and number of neurites were significantly increased in *Bfc* mutants (Supplemental Figure 10B). However, after 8 days in culture, the majority of homozygous neurons lost their integrity, while the extent of dendritic branching in *Bfc/+* neurons was dramatically lower than in controls (Figure 7, A and B). Moreover, the depolarizing effect of high  $K^+$  on dendritic arborization and neurite length was inhibited in *Bfc/+* neurons (Supplemental Figure 11). As the identified human de novo  $\beta$ -catenin mutations would generate mRNAs undergoing non-sense-mediated decay and consequently result in *CTNNB1* haploinsufficiency, we studied the effect of reduced  $\beta$ -catenin expression on neuronal development. To this aim, we transfected primary neuronal cultures obtained from WT mice with an siRNA against *CTNNB1*. Transfection of this siRNA decreased  $\beta$ -catenin expression by 54% in WT cultures (Figure 7D), thus closely mimicking the reduction expected in patients bearing  $\beta$ -catenin mutations. Compatible with the reduction in neurite extension observed in neuronal cultures from *Bfc* mutant mice (Figure 7B), siRNA-mediated  $\beta$ -catenin knockdown in WT cultures produced a significant decrease in neurite length and in the number of processes compared with cultures transfected with a control siRNA (Figure 7D), indicating the pivotal role of  $\beta$ -catenin in shaping neuronal architecture.

*Timing and decision making is distorted in Bfc mutants.* To test timing in cognitive processing, we used a basic “peak procedure” paradigm (22) in which mice were trained to collect a reward at a particular time interval after a light event (Figure 6A). For trials in which rewards were given, responses increased significantly during the expected time interval in WT mice, but not in *Bfc/+* mutants (Figure 6B). Moreover, in probe trials where no reward was given, responses of *Bfc/+* mice during the critical time window were significantly lower than littermate controls (Figure 6B). Using an automated home-cage version of the peak procedure protocol (23), we recorded the animals’ performance through their regular sleep-wake cycle for several days. This more accurate analysis of temporal responses confirmed the learning deficit. We found no difference in the peak distribution between the first and last day of training in *Bfc/+* mice, while controls reduced their peak time and the spread of their temporal responses (Figure 6, C and D). We further investigated temporal behavior by identifying the “start” and “stop” indices from the cumulative distribution of nose pokes (Supplemental Figure 8) to assess anticipatory and perseverative behaviors, respectively. Interestingly, during training, *Bfc/+* mice did not moderate their response

**Figure 4**

Behavioral phenotypes of *Bfc/+* adult mice. (A) ASR in *Bfc/+* ( $n = 10$ ) mice is unaffected compared with that of controls ( $n = 10$ ). (B) Reduction in PPI is extremely robust, with significant reductions seen in *Bfc/+* mice. (C) Rotarod performance over 3 daily sessions is lower in *Bfc/+* ( $n = 10$ ) mice compared with controls ( $n = 10$ ), although their performance has improved by the third day. (D) Ultrasonic vocalizations are disrupted in *Bfc/+* ( $n = 10$ ) mice compared with littermate controls ( $n = 10$ ), with reductions in the total number of calls upon separation and in the average call duration. (E) Call complexity is also lower in mutants, with a significantly lower number of elements per call. (F) Representative ultrasonic vocalizations for WT mice and *Bfc/+* littermates. \* $P < 0.05$ , \*\* $P < 0.01$ , Student's  $t$  test.

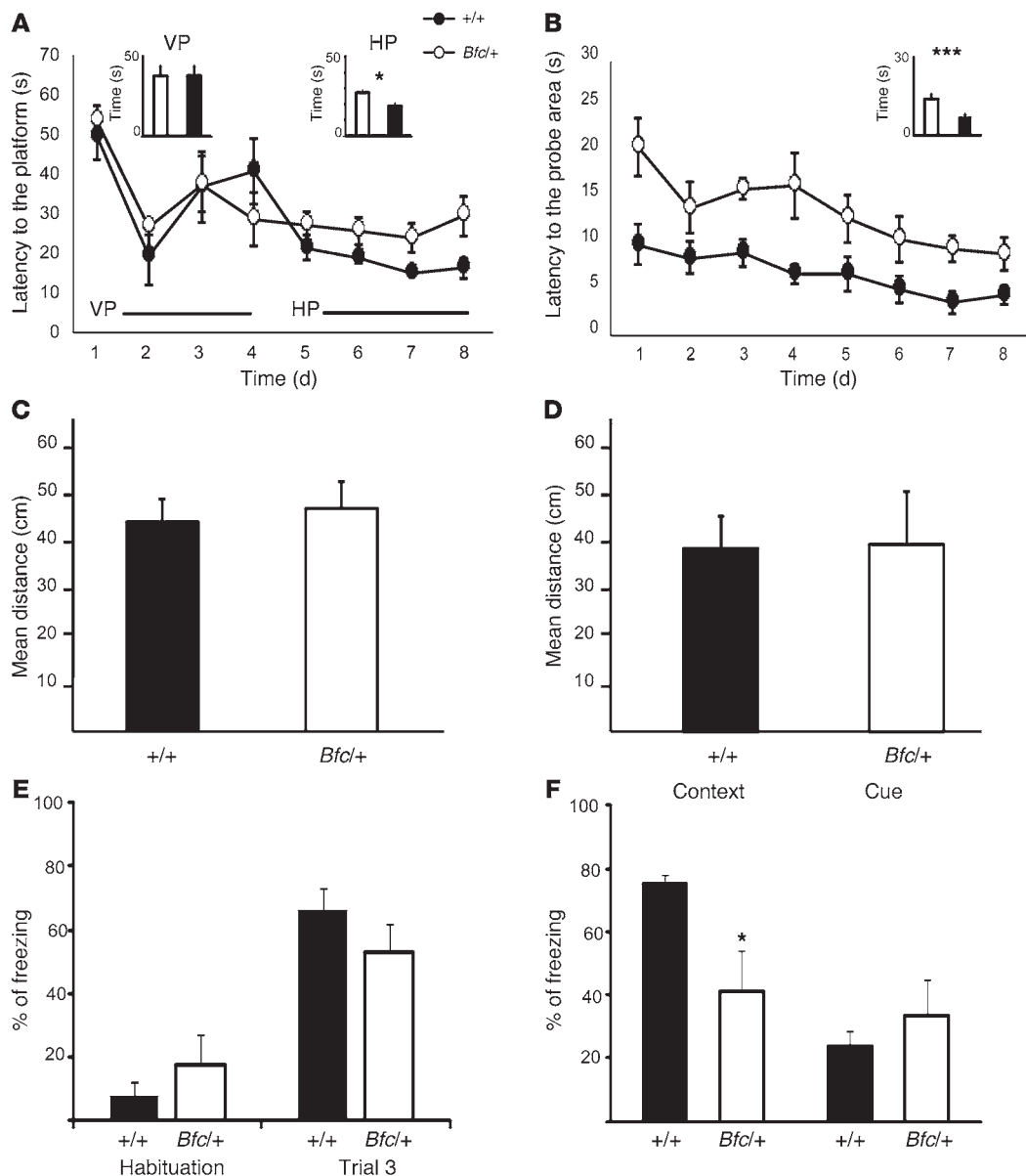
To determine whether structural changes could lead to functional differences at the scale of neuronal networks, we cultured hippocampal neurons on high-density multi-electrode arrays (MEA). The electrodes allowed us to record extracellular action potentials from up to 4,096 electrodes on a 2.67 mm<sup>2</sup> area. To identify functional differences among cultured networks, cell cultures were seeded at low density (Figure 7E) to obtain a sparse network coupled with the large-scale electrode array, thus achieving a high percentage of electrodes recording single units. Under these conditions, results from spike sorting showed that approximately 84% of selected electrodes recorded single units (Supplemental Table 1). Electrophysiological activity was recorded in the spontaneous condition and in the presence of bicuculline (BIC) to disinhibit the network. The cumulative distributions of network-wide activity parameters, i.e., mean firing rate (MFR) and mean bursting rate (MBR), are right shifted and are indicative of a higher excitability of networks from *Bfc/+* mice. Differences in the analysis of the mean burst duration (MBD) are less evident. This higher network excitability was also observed when we analyzed data by separating the spontaneous from the disinhibited data sets (data not shown). Further, the synaptic strength was evaluated based on outcomes from the functional connectivity estimation among a large number of single units in the network. Based on the analysis of the length of the strongest links within cultured networks (Figure 7I), we observed that *Bfc/+* neuronal networks maintain longer link lengths compared with controls. The link strength and

degree of connectivity were observed to be lower in *Bfc/+* networks (data not shown). This indicates that the functional connectivity in hippocampal neuronal networks formed from *Bfc/+* heterozygous mice, especially at the local circuitry level, is less efficient.

We determined whether functional differences in cultured neuronal networks might be related to ultrastructural anomalies in brains of adult *Bfc/+* mice. We performed electron microscopic analysis of cortical and CA1 hippocampal regions from adult brain sections. In heterozygotes, we observed a lower density of docked synaptic vesicles (SV) in cortex and CA1 (Figure 8, A and B). Lower SV density could thus indicate a lower release probability at *Bfc/+* synapses and hence a lower synaptic strength. To investigate this further, we recorded field-evoked postsynaptic potentials (fEPSPs) in the CA1 region of hippocampal slices, evoked by stimulating the Schaffer collateral pathway (Figure 8C). The slope of fEPSP in *Bfc/+* was not significantly different from that in controls (Figure 8D, 2-way ANOVA,  $P > 0.05$ ), nor was there a difference in the observed paired-pulse ratio (Figure 8E, 2-way ANOVA,  $P > 0.05$ ). We then investigated the effect of the mutation on synaptic plasticity and found that long-term potentiation (LTP) induced by either tetanic (Figure 8F) or  $\theta$ -burst (Figure 8G) stimulation was significantly reduced in slices from *Bfc/+* animals.

## Discussion

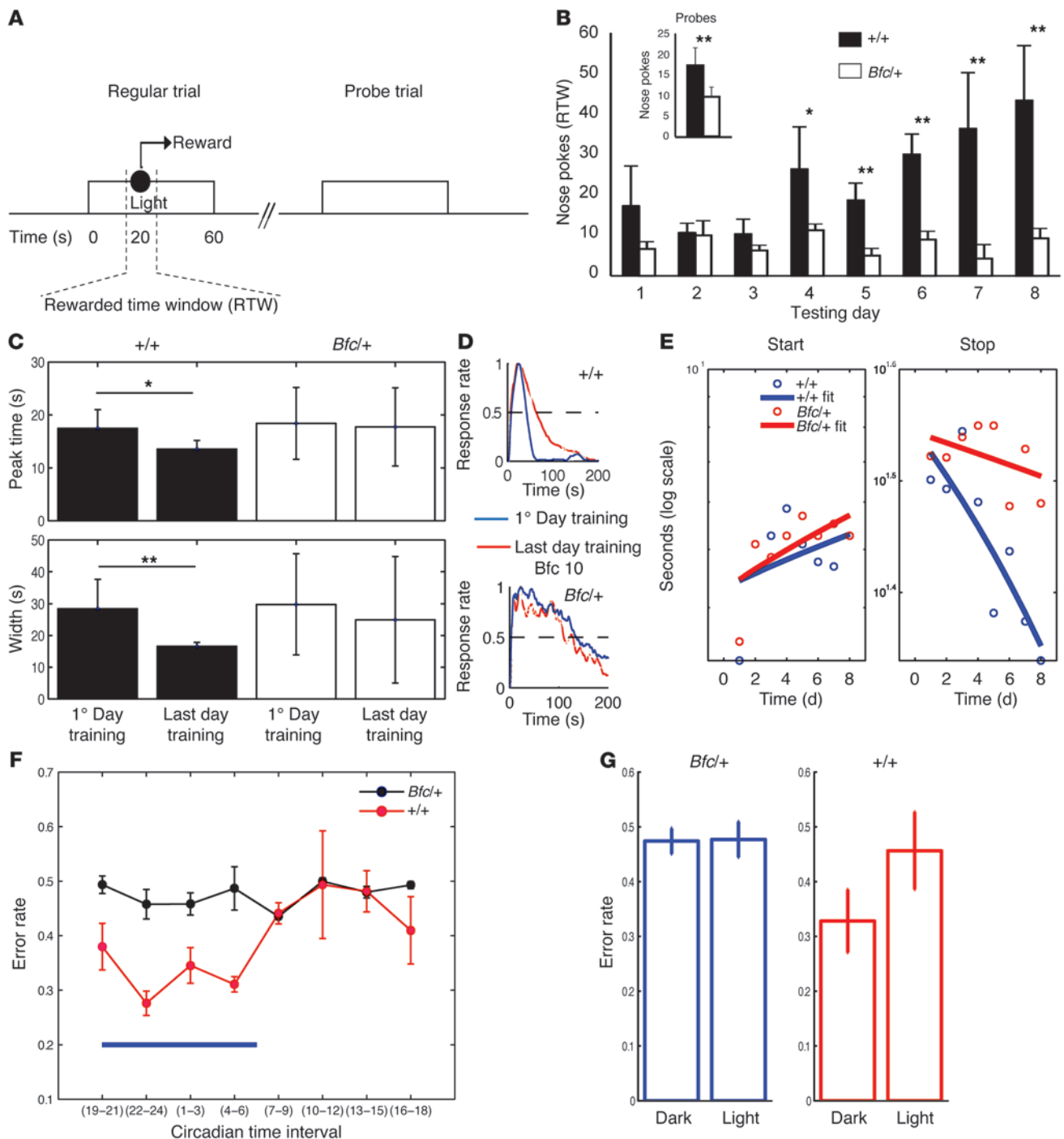
In this study, we have clearly shown that  $\beta$ -catenin plays key roles affecting brain function, morphology, and craniofacial features



**Figure 5**  
 A number of parameters of learning and memory are deficient in *Bfc/+* mice. WM test showing mean latencies to reach the escape platform are plotted for daily sessions over 8 training days (A) and for probes (B) in *Bfc/+* and littermate controls ( $n = 10$ ). Visible platform (VP) and hidden platform (HP) conditions are marked along the training. Mean distances for regular training (C) and probe (D) trials are plotted. In the fear conditioning test, freezing time during habituation and training (E) and exposure to the context and cue conditions (F) are presented for *Bfc/+* mice ( $n = 8$ ) and littermate controls ( $n = 8$ ). \* $P < 0.05$ , \*\*\* $P < 0.001$ ; Student's  $t$  test.

in both mouse and human. This underlines the recent proposal that the  $\beta$ -catenin protein-interacting network is important in abnormal neurodevelopmental etiology (12, 25). We were able to define a clinically recognizable syndrome in humans with a distinctive phenotype, including ID, ASD, microcephaly, and childhood hypotonia with progressive spastic diplegia, associated with de novo mutations in *CTNNB1*. The individual with the p.Thr551Met mutation in *CTNNB1* who was presented in the ASD study (12) may also fit in this clinical spectrum, since this person was described to have, in addition to ASD, a non-verbal IQ in the range of moderate ID (NVIQ 58). No further

clinical data were provided, however. Interestingly, our results are also in agreement with the finding that Wnt and  $\beta$ -catenin proteins are decreased in frontal cortex in post-mortem brain tissue of individuals with ASD. These deficits were associated with abnormal dendritic branching and reduced cell body size of astrocytes (26). Furthermore, the parallels in the phenotypic features with the mouse model, batface, strongly suggest shared common pathological mechanisms in morphologic and neurodevelopmental processes in human and mouse. Consequently, we have taken advantage of the batface mouse model to further explore the role of  $\beta$ -catenin in CNS functions and have

**Figure 6**

*Bfc/+* mice show deficits in temporal cognition. **(A)** The peak procedure task. Probes differ from normal trials, as the light stimulus is not followed by any reward. **(B)** Mean nose pokes for the rewarded time windows (RTWs) within each session are presented for normal trials over 8 consecutive days and all probe trials. *Bfc/+* mice ( $n = 12$ ) do not increase nose poking within the RTW as *+/+* mice do ( $n = 12$ ). **(C)** Timing responses are collected in a home-cage apparatus using separate mouse cohorts ( $n = 6$ ). Peak time and width (spread) decrease significantly between the first and last day in *+/+*, but not in *Bfc/+* mice. \* $P < 0.05$ ; \*\* $P < 0.01$ . **(D)** Peak distribution for the first (red) and last (blue) days for representative *+/+* and *Bfc/+* mice. **(E)** Start and stop times test anticipatory and perseverative behaviors. WT mice show a progressive optimization (increasing the start time and decreasing the stop time) in their responses, corresponding with reward delivery time. Interestingly, *Bfc/+* mice do not modify stop time responses, indicating a perseverative response within trials. **(F)** Timing is assessed for 2 intervals (short vs. long), and only correct responses are rewarded. Error rates are calculated and plotted in 3-hour bins; the blue bar represents the dark phase of the 12-hour light/12-hour dark cycle. A comparison of behaviors during the dark (active) and light (inactive) phases is shown for *Bfc/+* and *+/+* mice **(G)**. No phase differences in behavior are evident in *Bfc/+* mice, while the error rate significantly increases in WT animals in the light phase.

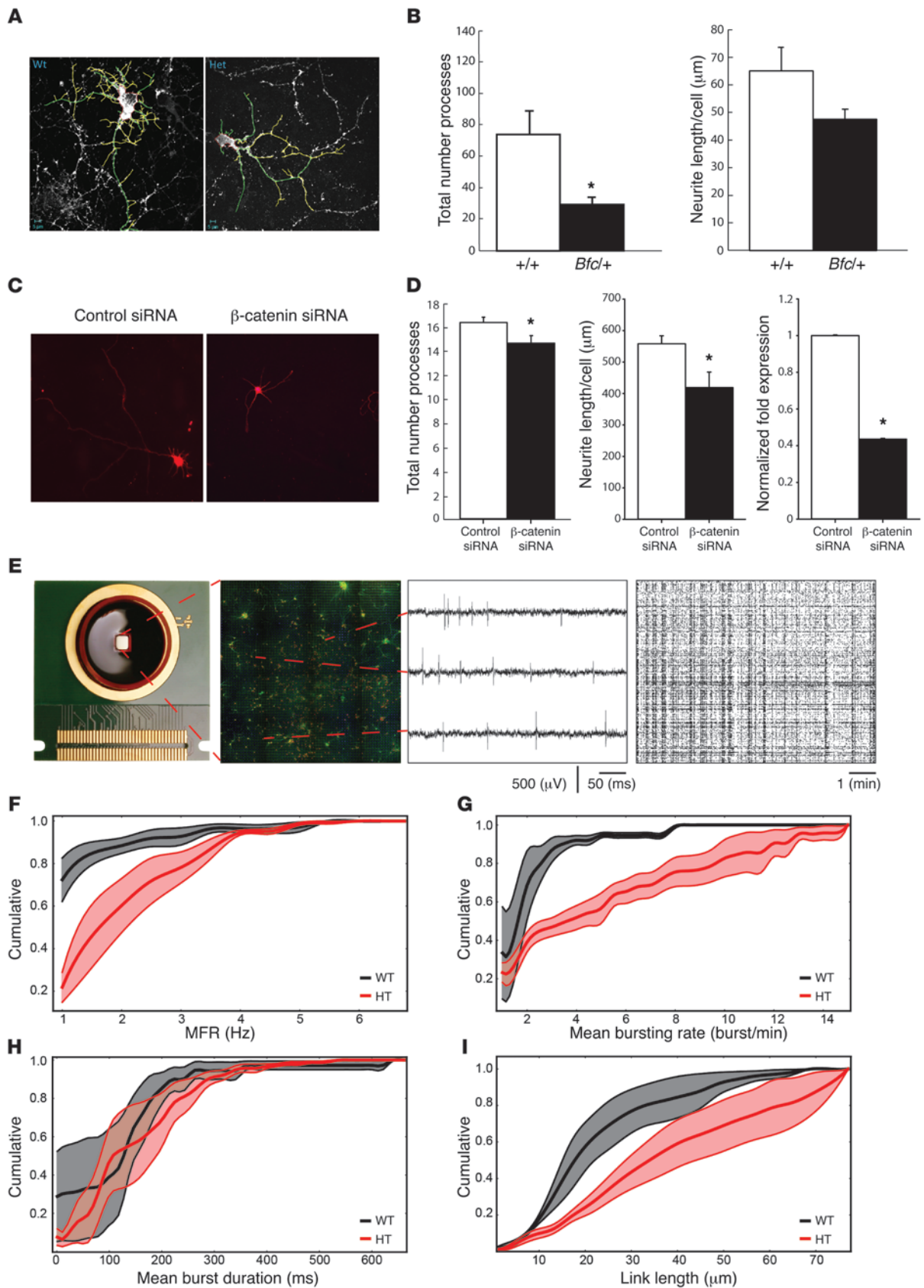




## Figure 7

Morphological and functional deficits in *Bfc*/*+* primary hippocampal neuronal cultures. **(A)** Representative images of primary cultures of *+/+* and *Bfc*/*+* hippocampal neurons after 8 days in culture. Scale bars are as indicated. Primary processes are shown in green, secondary processes in yellow. **(B)** Number of processes and neurite length are presented. Processes are significantly less in *Bfc*/*+* neurons. \* $P = 0.02$ , 2-tailed  $t$  test. **(C)** Representative images of neuronal cultures transfected at 1 DIV with  $\beta$ -catenin or control siRNA and fixed at 7 DIV. **(D)** siRNA against  $\beta$ -catenin efficiently decreased mRNA expression, as assessed by RT-qPCR ( $P < 0.01$ ), while neurite extension was significantly reduced (\* $P < 0.05$ ) in  $\beta$ -catenin-transfected neurons. **(E)** In vitro neuronal network set-up showing (left to right) the high-density MEA chip, fluorescence image of the low density culture ( $\beta_3$ -tubulin green, NeuN red) showing the sparse network distribution on a portion of the electrode array (black square), raw data traces of spiking activity acquired from 3 different channels, raster plot of approximately 400 active channels (i.e., firing rate  $> 0.1$  spike/s) showing synchronous firing and sustained bursting activity. **(F–I)** cumulative distributions of network parameters (*+/+* black,  $n = 4$ ; *Bfc*/*+* red,  $n = 6$ ). Bold lines and shaded regions correspond to mean  $\pm$  SEM. The *Bfc*/*+* cultures were more excitable, as evidenced by the higher MFR **(F)** and MBR **(G)**. Less evident is the variation for the MBD **(H)**. The functional connectivity analysis based on cross-correlation shows that functional link length was also higher in *Bfc*/*+* **(I)**.

identified specific molecular and synaptic deficits that could be responsible for the range of developmental, behavioral, and cognitive deficits seen.

The batface mutant expresses a unique phenotype that is a combined consequence not only of a gain in WNT-related function (15), but also, as we show here, a dominant-negative effect on adhesion-related function. For what we believe is the first time, this allows investigation of in vivo consequences of mutant  $\beta$ -catenin function in adult heterozygotes. Although specific embryonic brain deficits have been noted in conditional null mutants including, in some cases, abnormalities in development of the corpus callosum (27–29), none of these studies have focused on postnatal mutant phenotypes, nor have they noted dysmorphisms or behavioral deficits in heterozygotes. Although the lack of deficits in heterozygous loss-of-function mouse mutations does not seem consistent with the severe phenotype associated with  $\beta$ -catenin loss-of-function in humans, Huelsen et al. (30) suggested that plakoglobin can assume  $\beta$ -catenin's adhesive role in its absence. This might not only explain the apparent differences in loss-of-function mutations in mouse and humans, but may also account for the unique nature of the *Bfc* mutation. Given the continued ability of mutant  $\beta$ -catenin to interact with the cytoskeleton and with other protein partners, the presence of the *Bfc* mutant protein is likely to inhibit the ability of plakoglobin to assume its compensatory adhesive role in heterozygous animals.

As a testament to the complex network of CTNNB1 and its interacting partners, the severity of the batface mutation and its pleiotropy can vary as a function of genetic background. On any congenic background investigated in this or in previous studies (15), the viability of heterozygous embryos and fertility of adults are compromised, although craniofacial dysmorphisms and some behavioral traits are robust and found to be insensitive to background (data not shown). To produce sufficient cohorts of animals for this study, we chose to use animals of mixed genetic background. This did not affect our analysis of behavioral parameters, although we did see the appearance of the low penetrance corpus callosum anomaly in a small number of animals.

In terms of its specific molecular lesion, the closest mutant to the one described here is a targeted phosphomimetic mutation (Tyr654Glu) (31). Murase et al. (8) provided fundamental evidence that the Tyr654 phosphorylation state is vital in coordinating activity-induced presynaptic and postsynaptic plasticity. As the effects of the *Bfc* mutation appear to mimic that of Tyr654 phosphorylation, our synaptic morphological and functional results are consistent with the expected specific abnormalities at the synaptic junction and at the network level. There are also many phenotypic similarities between *Bfc* and Tyr654Glu, including an anterior truncation and late embryonic lethality in homozygotes and a reduced interaction with cadherins. However, the Tyr654Glu mutation expresses a far stronger gain-of-function in WNT signaling, and this is particularly relevant when comparing adult heterozygous phenotypes, as unlike the *Bfc*/*+* mice, Tyr654 heterozygotes have no documented craniofacial phenotype and show increased tumor initiation with intestinal adenomas.

Differences between the *Bfc* and Tyr654Glu mutants may be related to different capabilities of the 2 mutants to undergo nuclear import and export, processes that are also particularly sensitive to the Tyr654 phosphorylation state (32). Similarly, amino acid substitutions in Arm12 can influence the ability of this repeat to interact with the C-terminal domain of  $\beta$ -catenin. Helix C can fold back on Arm12, blocking the binding of transcriptional coactivators to this area, while phosphorylation of Tyr654 prevents this fold back, leading to the subsequent phosphorylation of Ser675 and the recruitment of transcriptional coactivators, including CBP and TBP (33). Y654E mutants do show an increased sensitivity to Ser675 phosphorylation; however, although we could not determine Ser675 phosphorylation state in *Bfc*/*+* mice, we did not detect any change in the ability of the mutant protein to interact with the transcriptional coactivator CBP (data not shown). Such subtle differences in the functions of the 2 mutant proteins could underlie the discrete phenotypic consequences observed.

The deficits in cultured *Bfc* hippocampal neurons are consistent with studies overexpressing  $\beta$ -catenin. Expression of stabilized  $\beta$ -catenin increased dendritic growth and arborization, but this effect was inhibited by coexpression of the intracellular domain of N-cadherin that sequesters  $\beta$ -catenin (34). Moreover, the depolarizing effects of high  $K^+$  on dendritic arborization and neurite length were inhibited either by overexpression of the dominant-negative form of N-cadherin or by the presence of the *Bfc* allele. Critically, these effects have been shown to be independent of Wnt-related transcriptional changes, although Wnt-induced stabilization of  $\beta$ -catenin may be important in mediating depolarization-induced changes.

The cadherin/ $\beta$ -catenin complex has previously been demonstrated to play a role in the recruitment and localization of SVs to synapses (8), and  $\beta$ -catenin is important for controlling the size and localization of the vesicle cluster. In fact, the deletion of  $\beta$ -catenin in hippocampal pyramidal neurons has been associated with a decrease in the density of vesicles of the reserve pool. We have shown that the overall functional connectivity of *Bfc*/*+* is less strong with respect to WT dissociated networks. In particular, local connectivity among neurons seems to be mostly impaired, probably due to inefficient synapses, thus compromising the reliability of the signal transmission. This loss in efficiency explains why *Bfc*/*+* network activity is higher both for single spikes and bursting activity.

The conclusions of our study support a central role of  $\beta$ -catenin/cadherins interactions in the molecular machinery that regulates synaptic plasticity and neuronal network connectivity. We envisage

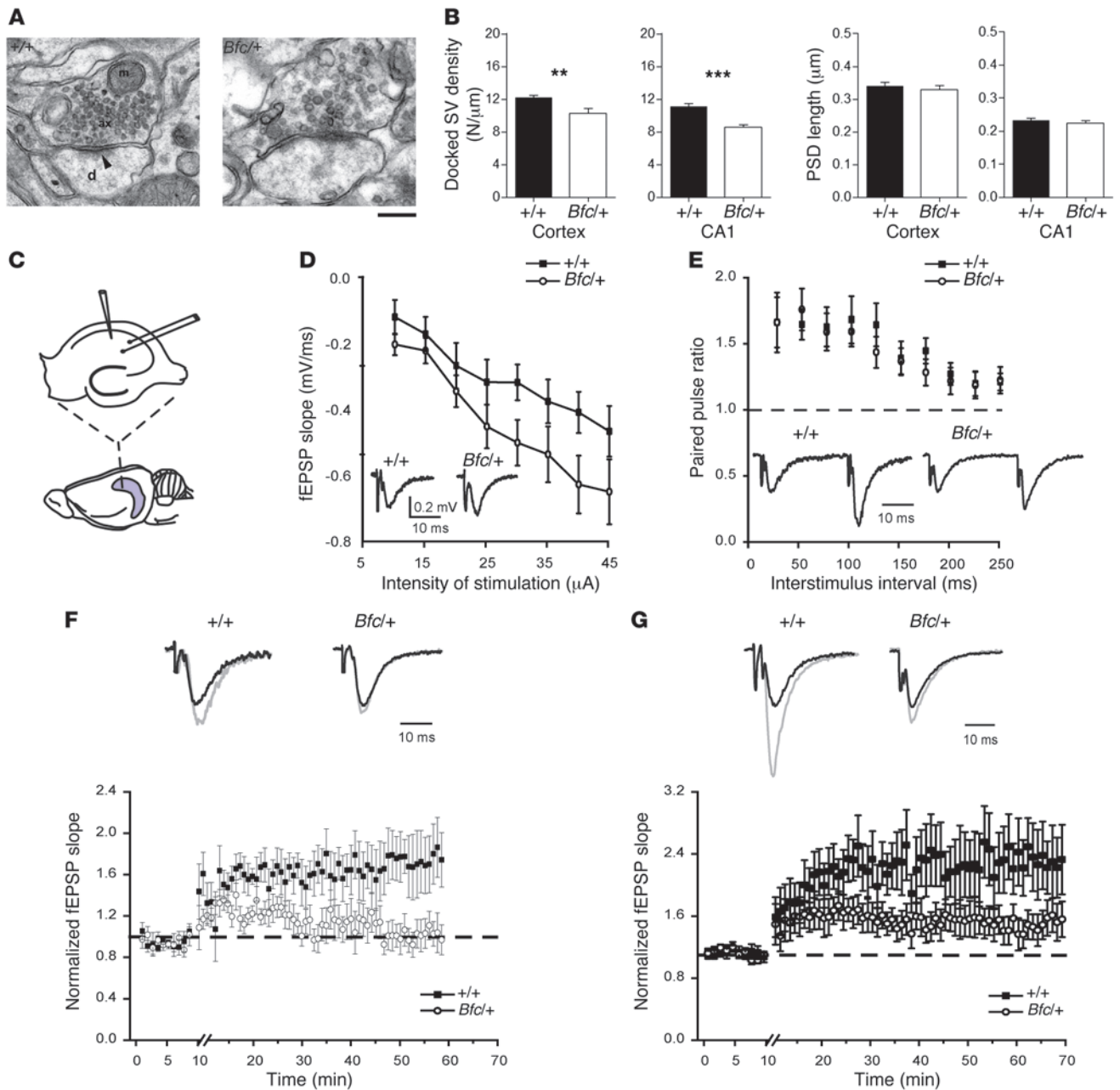


**Figure 8**

Morphological and functional synaptic deficits in *Bfc/+* adult hippocampus. **(A)** Representative electron microscope images from WT and heterozygous CA1 synapses; images show a section of a presynaptic axonal bouton (ax) containing the cluster of SVs and mitochondria (M) and the dendrite of a postsynaptic neuron (D); the postsynaptic density (PSD) is also visible (arrowhead). Scale bar: 200 nm. **(B)** Quantification of membrane-docked SV density (vesicles/ $\mu$ m) and PSD length ( $\mu$ m) was performed for 142 CA1 and 128 cortical +/+ ( $n = 3$ ) and 152 CA1 and 115 cortical *Bfc/+* ( $n = 3$ ) excitatory presynaptic terminals using ImageJ. **(C)** Experimental configuration used to perform electrophysiological recordings in adult hippocampal slices. **(D)** Slope of the fEPSP as a function of injected current recorded in hippocampal slices from WT (black squares,  $n = 7$  mice, 10 slices) and *Bfc/+* (white circles,  $n = 7$  mice, 10 slices) animals. Representative traces are shown (inset). **(E)** Paired-pulse ratio as a function of the interstimulus interval for WT ( $n = 7$  mice, 9 slices) and *Bfc/+* ( $n = 7$  mice, 9 slices) mice. Traces (inset) are normalized to the first stimulus fEPSP amplitude. **(F and G)** Slope of the fEPSP before and after tetanic **(F)** or  $\theta$ -burst **(G)** stimulation in WT (black squares) and *Bfc/+* (white circles) slices. Values are normalized to the fEPSP slope value under control conditions. **(F)** WT,  $n = 5$  mice, 5 slices; *Bfc/+*,  $n = 5$  mice, 6 slices. **(G)** WT,  $n = 4$  mice, 5 slices; *Bfc/+*,  $n = 5$  mice, 6 slices. Traces (inset) are normalized to the amplitude of the fEPSP under control conditions. \*\* $P < 0.01$ , \*\*\* $P < 0.001$ .



that our genetic model can result in a wealth of understanding in the molecular machinery that underlies  $\beta$ -catenin's role in controlling synaptic changes and, ultimately, cognition. Furthermore, our ability to probe  $\beta$ -catenin function in this mouse model could also allow us to understand and perhaps treat a spectrum of human disorders associated with defective neurodevelopment including ID and ASD.

## Methods

### Patient recruitment

The present 4 individuals had been referred to the department of Human Genetics, Radboud University Medical Centre, for the evaluation of their moderate to severe ID. In all individuals, a clinical evaluation, followed by specific DNA diagnostic tests on indication and SNP array analysis, had been performed previously. These results were all normal. Subsequently, 2 of the individuals (patients 2 and 4) were considered for family-based whole exome sequencing (WES) studies (trio-analysis). Results in patient 2 were recently reported by our group (trio 70, de Ligt et al.; ref. 13). Results in patient 4 were not previously reported. Patients 1 and 3 were included in a confirmation series of 765 persons with ID in which we used high-throughput resequencing to screen new candidate genes, including *CTNNB1*, as described in the same publication by our group (3rd and 2nd patient with *CTNNB1* mutation, Supplemental Figure 7 and de Ligt et al.; ref. 13).

### Animals

Animals were genotyped using a TaqMan allelic discrimination assay under standard conditions. Primers used were as follows: 5'-TGGCCTCAAGGGC-TAGTTTCT (forward) and 5'-TGAAAGCCGCTTCTGTGAATC (reverse). TaqMan MGB probes were as follows: FAM-TTTATTCCAGCAACATAC (WT) and VIC-TTTTATTCCAGCAAATA (mutant). To maintain the fertility and fecundity of the *Bfc* mutant line, animals were bred by crossing heterozygotes on a congenic C57BL/6J background to C3H/HeH mice. Mutant F1 progeny were subsequently crossed to WT F1 animals to generate test cohorts. Unless otherwise stated, separate cohorts were used for all phenotypic analysis and as a source of all tissues in the current study. Following behavioral tests, animals were sacrificed and any animals showing gross anatomical defects were excluded from the study. X-rays were determined using the pDEXA Sabre X-ray Bone Densitometer (Norland Medical Systems). Briefly, mice were anesthetized and placed in the apparatus; scanning was performed at a speed of 40 mm/s and a resolution of 1.0  $\times$  1.0 mm/s (HAV: 0.020). Bone measurements were determined using associated software.

### 3D modeling of $\beta$ -catenin and E-cadherin

The atomic coordinates of the crystal structure of the  $\beta$ -catenin/E-cadherin complex (PDB 117X) (5) and the full-length crystal structure of  $\beta$ -catenin (PDB 2z6h) (2) were downloaded from the Protein Data Bank and visualized using PyMOL (PyMOL Molecular Graphics System, version 1.3, Schrödinger LLC; <http://www.pymol.org/>). Using the IntFOLD2 fold recognition method (35, 36), a full atomic 3D model was generated for the  $\beta$ -catenin sequence containing the point mutation Thr653Lys in the Arm12 domain. The phosphorylated tyrosine side chain (Tyr654-p) in the  $\beta$ -catenin WT structure was modeled using the Builder tool in PyMOL. The 2Z6H  $\beta$ -catenin crystal structure was superimposed with the original  $\beta$ -catenin chain in 117X to show the protein in full-length complexed with the E-cadherin structure. Likewise, the IntFOLD2 model of  $\beta$ -catenin was superimposed with the original  $\beta$ -catenin crystal structure of WT  $\beta$ -catenin to show the Thr653Lys mutant residue. The side chain orientations that would depict the greatest steric clashes of Tyr654-p and Thr653Lys were chosen from all possible rotamers. For this, the Mutagenesis tool of PyMOL was utilized.

### Cell transfection, protein immunoprecipitation, electrophoresis, and Western blotting

HEK293T cells were cotransfected with N-cadherin-EGFP (plasmid #18870; Addgene) and either WT- $\beta$ -catenin-V5/His or *Bfc*- $\beta$ -catenin-V5/His (gifts from R. Arkell and A. D'Cruz, Australian National University, Acton, Australia) full-length cDNA constructs (1  $\mu$ g of each) using jetPEI reagent (Source Bioscience); these were cultured for 48 hours. Cultured cell extracts ( $n = 3$  per group) or whole hippocampus samples ( $n = 7$  per genotype) were prepared by lysis in RIPA buffer as described previously (37). Immunoprecipitation (IP) of N-cadherin/ $\beta$ -catenin complexes from whole hippocampus extracts was performed using Dynabeads-Protein G Immunoprecipitation Kit (Invitrogen) according to the manufacturer's instructions. For IP, 0.2 mg of lysate was used and 30% of the eluted complex was loaded on polyacrylamide gels. As reference, 10  $\mu$ g of total lysate was also loaded. Electrophoresis was performed using the Invitrogen system and then transferred to nitrocellulose membrane using the iBlot (Life Technologies). Membranes were blocked for 1 hour in blocking solution (5% skimmed milk in PBS + 0.1% Tween 20) and then incubated in primary antibody diluted in blocking solution overnight at 4°C. After extensive washing in PBS plus 0.1% Tween 20, membranes were incubated for 1 hour in the corresponding secondary antibody diluted in blocking solution and washed as before. For protein stability and IP studies, an antibody to the C-terminal end of  $\beta$ -catenin (ab16051; Abcam) and an antibody to N-cadherin (ab18203; Abcam) were used. Control IPs were carried out using normal rabbit IgG (sc-2027; Santa Cruz Biotechnology Inc.). Secondary antibodies used were goat-anti-rabbit IgG-HRP (A6154; Sigma-Aldrich) and goat-anti-mouse IgG-HRP (A4416; Sigma-Aldrich). For IP of transfected cells, lysates were incubated with anti-GFP monoclonal antibody (Roche) at 4°C overnight, followed by protein G-sepharose (P3296; Sigma-Aldrich) at 4°C for 1 hour, after which beads were washed 3 times with RIPA buffer. Control IPs were carried out in the absence of transfected N-cadherin. Immunoprecipitated proteins were eluted from the beads by boiling in LDS buffer (Life Technologies) for 5 minutes. For quantitative 2-color Western blot analysis, blots were probed with both anti-GFP (Santa Cruz Biotechnology Inc.) and anti-V5 (Life Technologies) antibodies, washed, and incubated with IR fluorophore-conjugated secondary antibodies, IRDye 800 and IRDye 700, as described previously (37). Simultaneous 2-color detection performed using an Odyssey infrared imaging system (LI-COR Biosciences). Quantitation of  $\beta$ -catenin-V5 in the immunoprecipitate was performed using Odyssey imager software, normalized to N-cadherin-EGFP fluorescence.

### MRI

High-resolution T2-weighted and diffusion-weighted MR imaging of mouse brains was performed at 7 Tesla on paraformaldehyde-fixed specimens using the following parameters: 3D fast spin-echo (TR = 550 ms, TE = 33 ms, echo spacing 11 ms, voxel size of 0.094 mm<sup>3</sup>); diffusion weighted images (81 gradient orientations,  $b = 1225$  s/mm<sup>2</sup>,  $\delta = 5$  ms,  $\Delta = 10$  ms, voxel size 131  $\times$  131  $\times$  500  $\mu$ m, TR = 7500 ms, TE<sub>eff</sub> = 23 ms). Male *Bfc*/ $+$  ( $n = 10$ ) and control WT littermates ( $+/+$ ;  $n = 9$ ) were used. Volumes of anatomical labels were computed using a registration-based approach using 2 average reference templates, one for *Bfc*/ $+$  and one for control subjects. Each template was manually labeled into anatomical regions and the volume of specific anatomical regions in individual subjects was obtained via a symmetric diffeomorphic registration algorithm (38). Diffusion-tensor Imaging (DTI) tractography was performed as follows: DWI images were first resampled to obtain isotropic voxels (129  $\mu$ m<sup>3</sup>) and nonbrain tissue manually removed. Fractional anisotropy (FA) images were created by fitting a tensor model to the raw diffusion data using FMRIB software library,



v5.0 (FSL). Estimates of axonal fiber projections were computed using a deterministic fiber assignment by continuous tracking algorithm. Criteria for terminating the tracking of individual fibers included an anisotropy threshold (values below 0.15) and a maximum stiffness condition, so that the tracking was terminated when the diffusion directions in consecutive steps differed by more than 40°.

### ASR and PPI

ASR and PPI were measured in *Bfc/+* ( $n = 10$ ) and *+/+* ( $n = 10$ ) mice using standard acoustic startle devices (Med Associates). For the startle response, the session consisted of a 5-minute acclimation period followed by five 110-dB white noise pulses. Responses were expressed in arbitrary units and averaged. Duration of pulses were 10 ms and the inter-trial interval (ITI) was 25 seconds on average (20–30 seconds). For PPI, animals received a white noise pulse alone (110 dB) preceded by a 60-dB prepulse. The background noise was set at 45 dB. The interval between prepulse and pulse was 50 ms. Each trial was presented a total of 15 times with pseudorandom ITI. The test was conducted in dim light. The amount of PPI was measured in the prepulse plus startle trial types and expressed as percentage of the basal startle (19).

### Rotarod

*Bfc/+* ( $n = 10$ ) and *+/+* ( $n = 10$ ) mice were challenged to keep their balance on a rotating rod. The latency period before falling off the rod was then measured and evaluated as a measure of their performance. After an initial training phase (2 minutes) in which all mice were familiarized with the test at a constant speed (4 rounds per minute [rpm]), the accelerating protocol was set from 4 rpm to 40 rpm. We submitted different cohorts of *Bfc/+* ( $n = 10$ ) and *+/+* ( $n = 10$ ) mice to 1 extensive session once a day for 3 days. Each session included 6 consecutive phases of 1 minute each. Three phases were accelerating phases from 4 to 40 rpm and 3 were stable phases at 4 rpm. The stable and the accelerating phases were alternated and all mice started the session with a stable phase.

### Ultrasonic vocalization

Ultrasound vocalizations are emitted when a pup is isolated from the nest, its mother, and littermates (39). Six-day-old pups ( $n = 10$  per genotype) were gently handled by the experimenter so as to remove 1 pup at a time from its cage and place it in an isolated cage where a microphone sensitive to ultrasonic sounds was set. The microphone was connected via an Avisoft UltraSoundGate 116 USB audio device to a personal computer. The monitoring occurred at room temperature, and the length of time of recording of ultrasounds was 5 minutes.

### WM

In this test, *Bfc/+* ( $n = 10$ ) and *+/+* ( $n = 10$ ) mice were trained to locate a submerged or a visible platform within a tank of opaque water by using strategically placed visual cues. On the day prior to starting the experiment, mice were placed on the platform for a 1-minute session to allow for orientation. Following this, on days 1 to 4, mice were placed in the water and were subjected to blocks of 4 trials with a 10- to 15-minute ITI. A visible platform was placed just above the water, and mice that found the platform within the allotted time remained there for 20 seconds. Mice that did not locate the platform within the allotted time were manually placed there. At the end of each day, the platform was removed and the mouse was placed in the tank for 1 minute (probe trial). From day 5 to 8, all mice were subjected to daily sessions as described above, but in this case, the platform was hidden just below the water. On day 9, the position of the platform was changed and the session was repeated. The locomotor activity of the mice was monitored by a video tracking system (Ethovision; Noldus).

### Fear conditioning

Mice ( $n = 8$  per group) were tested using a fear-conditioning protocol to test contextual memory. All mice were tested by means of the MultiConditioning System (TSE). The arena was 400 × 400 × 900 mm (w × d × h), and the house light was maintained at around 80 lux. After 120 seconds of habituation, mice were exposed for 28 seconds to the context serving as a conditioned stimulus, followed by an electric shock (2 s, 0.5 mA) representing the unconditioned stimulus for 3 trials separated by a 90-second interval. The memory test was performed 24 hours later, by reexposing the mice to the same context for 5 minutes, and 48 hours later, by reexposing the mice to the cue stimulus. Freezing was defined as a lack of movement besides respiration. The mean time of freezing behavior was expressed as a percentage of freezing in relation to the duration of test.

### Timing learning

We subjected mice to a series of cognitive timing tests to assess both the capability of memorizing a reward event and to localize it in time. For the purpose of this experiment, we used classical and novel (home cage) operant systems (TSE Systems), which are based on the nose-poking activity of the animal.

*Experiment 1: out-of-cage testing and peak procedure task.* *Bfc/+* ( $n = 12$ ) and *+/+* ( $n = 12$ ) mice were subjected to a 1-hour training session in a classical operant chamber every day for 8 consecutive working days as previously described (40). A central-hole LED and a 60-dB background white noise signalled the beginning of each trial. When mice nose-poked the control station, the central-hole LED and the white noise were switched off and the target lateral hole, working as a feeding station, was illuminated for 20 seconds (Figure 6A). After the first 10 seconds, a 20-mg food pellet reward was available at the feeding station mounted in the lateral hole. The ITI within the session was 40 to 50 seconds. In addition to the reward-based trials, a series of probe trials (in which no reward was delivered) was included. These occurred randomly during each session on an average of 1 out of 5 trials.

*Experiment 2: home cage-automated testing and switch task.* Six *Bfc/+* and 6 *+/+* mice were maintained in the home cage (equipped with a novel 3-hopper operant wall from TSE) to perform in the switch task as described previously (23). Briefly, all trials were self initiated by the animals by nose poking in 1 hopper (located in the middle of the operant wall) in the home cage. The rewards were delivered through the 2 lateral hoppers; 1 hopper was always associated with short light signals, while the other hopper was always associated with long light signals. The rewards were obtained only if the first nose poke of the animal occurred at the correct location following the specific signal. We trained all mice to a steady-state performance; all analyses were performed keeping a 1:2 ratio between short- and long-signals (3 vs. 6 seconds, respectively). The test included 20% nonrewarded (probe) trials to independently test the timing uncertainty. Number of errors as well as switch latencies, time accuracy, and time precision describe timing cognitive endophenotypes in this test (as described in refs. 23, 24).

### Primary neuronal cultures

Primary neuronal cultures were carried out both at IIT and the MRC. For the study of *Bfc/+* and WT neurons, embryos obtained from dams on a hybrid C57BL/6J × C3H/HeH background at E14.5 were dissected to obtain the hippocampus. Tissue was collected in neurobasal medium (Invitrogen) on ice, digested for 20 minutes with trypsin (0.25%) at 37°C, and subsequently washed several times. Before plating, cells were resuspended by pipetting them gently up and down. Cells were allowed to grow in 24-well plates on glass coverslips coated with poly-D-lysine (Sigma-Aldrich) and laminin (Invitrogen) in neuronal growth medium, consisting of neurobasal medium containing 1% L-glutamine, 1% penicil-



lin/streptomycin, and 2% B-27 supplement, in a standard cell culture incubator. DiI (1,1'-dioctadecyl-3,3,3',3'-tetramethylindocarbocyanine perchlorate; Invitrogen) was used to label the cultured neurons, and samples were subsequently embedded with ProLong (Invitrogen) mounting medium containing DAPI. Stained primary neurons were visualized using a LSM 710 confocal microscope (Zeiss) with a  $\times 63$  objective (Plan-Apochromat 63 $\times$  NA 1.4). Measurements of dendrite ( $n = 6$  per genotype) length and number for both *Bfc/+* and siRNA cultures were analyzed using the associated software (ZEN 2010, release 6.0.0.320).

### siRNA transfection and qPCR expression

For siRNA experiments, neurons were obtained from C57BL/6J embryos at E17.5. Cortical neurons at 1 day in culture (DIV) were transfected with Silencer Select Pre-designed siRNA against  $\beta$ -catenin (siRNA ID#: s63417) or control siRNA (both from Invitrogen) using Lipofectamine RNAiMAX Transfection Reagent (Invitrogen) according to the manufacturer's protocol. Cells were analyzed for  $\beta$ -catenin expression or neurite extension at 7 DIVs. RNA extraction, reverse transcription, and quantitative RT-PCR (RT-qPCR) were performed as previously described (41). Gene expression data were normalized by the multiple internal control gene method with GeNorm algorithm (42).  $\beta$ -Catenin (*Cttnb1*) expression data were normalized to *Ppia* and *Gapdh* reference genes. Primer sequences were as follows: GAPDH (forward): 5'-GAACATCATCCCTGCATCCA-3'; GAPDH (reverse): 5'-CCAGTGTGAGCTTCCCGTTCA-3'; PPIA (forward): 5'-CACTGTGCGTTTTGCGCCGTTG-3'; PPIA (reverse): 5'-TTTCTGCTGTCTTTGGAACCTTGTCTGC-3'; *Cttnb1* (forward): 5'-CAATGGCTTGGAATGAGACT-3'; *Cttnb1* (reverse): 5'-CCGTATCCACCAGAGTGAA-3'.

### High-density MEA

The high-density MEA platform (3Brain GmbH) was described in previous papers (43, 44). Briefly, these MEAs are monolithic CMOS devices able to simultaneously record extracellular electrophysiological signals from 4,096 electrodes at a sampling frequency of 7.7 kHz/electrode. Electrodes are squared (21  $\mu$ m side) and are arranged in a 64 by 64 array (pitch 42  $\mu$ m, 580 electrode/mm<sup>2</sup>). These chips allow the characterization of network activity in sparse cultures with an unprecedented spatial and temporal resolution. Primary hippocampal neurons from mouse embryos were dissociated at E14.5 and cultured on the APS MEAs. Chips were sterilized for 20 minutes in ethanol 80% and coated with a layer of poly-ethyl-imide (PEI). Each embryo was dissected separately, and 50  $\mu$ l of cell suspension was dropped on the recording area of each chip (about 200 cells/ $\mu$ l). After cellular adhesion, chip reservoirs were filled with 1.5 ml of Neurobasal (Invitrogen) and were maintained in an incubator until recordings. After 14 days in vitro, network activity was recorded for 10 minutes, both in basal conditions and after adding 30  $\mu$ M of BIC.

For the analysis ( $n = 4$ ,  $+/+$ ;  $n = 6$ , *Bfc/+*), we used the precise timing spike detection (PTSD) algorithm for spike detection (45) and custom Python scripts. All further analyses on the spike trains were computed by custom scripts in Python. In particular, bursting activity was detected with a single channel spike train burst detector (46) and network-wide activity was characterized by MFR, MBR, and MBD, computed only on active channels (i.e., firing rate > 0.1 Hz). Functional connectivity analysis was performed by crosscorrelating spike events among electrodes, and the strongest (i.e., most correlated) 100 to 200 links were considered.

### Electron microscopy

*Bfc/+* ( $n = 3$ ) and  $+/+$  ( $n = 3$ ) mice were anesthetized deeply with 20% urethane (0.1 ml/10 g) and perfused transcardially with ice-cold physiological saline for 3 to 4 minutes followed by a 0.1 M sodium cacodylate buffer containing 2% paraformaldehyde and 2% glutaraldehyde (pH 7.4). Brains were

subsequently sliced coronally (350  $\mu$ m) on a vibratome, and the regions of interest were cut into small pieces and post-fixed in 1% OsO<sub>4</sub>, 1.5% K<sub>4</sub>Fe(CN)<sub>6</sub>, and 0.1 M sodium cacodylate and en-bloc stained with 1% uranyl acetate in 20% ethanol. Finally, samples were dehydrated and embedded in epoxy resin (Epon 812; TAAB). Ultrathin sections were stained with 1% uranyl acetate and Sato's lead citrate and observed with a JEOL JEM-1011 microscope operating at 100 kV. Images were acquired with an ORIUS SC1000 CCD camera (Gatan). Synaptic area, SV number, and active zone (AZ) length were quantified using ImageJ software. Statistical significance was determined using unpaired Student's *t* test (GraphPad Prism 5.0).

### LTP experiments

Adult (12-week-old) mice ( $n = 7$  per genotype) were anesthetized with urethane (Sigma-Aldrich) and decapitated. The brain was quickly removed and sliced with a vibratome (VT 1000M; Leica) in ice-cold cutting artificial CSF (ACSF), containing: 250 mM sucrose, 25 mM NaHCO<sub>3</sub>, 25 mM glucose, 2.5 mM KCl, 1.25 mM NaH<sub>2</sub>PO<sub>4</sub>, 1 mM CaCl<sub>2</sub>, and 1.5 mM MgSO<sub>4</sub>, pH 7.3, saturated with 95% O<sub>2</sub> and 5% CO<sub>2</sub>. Coronal hippocampal slices (350  $\mu$ m thickness) were recovered at room temperature for at least 2 hours before the beginning of the experiment in recording solution containing: 125 mM NaCl, 25 mM NaHCO<sub>3</sub>, 25 mM glucose, 2.5 mM KCl, 1.25 mM NaH<sub>2</sub>PO<sub>4</sub>, 2 mM CaCl<sub>2</sub>, and 1.5 mM MgSO<sub>4</sub>, pH 7.3, saturated with 95% O<sub>2</sub> and 5% CO<sub>2</sub>. Electrophysiological experiments were performed in a submerged chamber. fEPSPs were recorded in the stratum radiatum of the CA1 region with a glass micropipette (resistance 1–2 megaohms), which was filled with recording ACSF. Current stimulation pulses were applied to the Schaffer collaterals pathway via a concentric bipolar tungsten electrode (FHC) placed at least 300 microns away from the recording electrode. Basal synaptic transmission was monitored at 0.067 Hz for at least 10 minutes (stimulation strength was set to 50% of the stimulation value generating maximal fEPSP slope). LTP was induced by  $\theta$ -burst stimulation (TBS, 4 TBSs with inter-TBS interval of 20 seconds; each TBS consisted of 4 bursts at 100 Hz delivered at 6 Hz; burst duration, 30 ms) or tetanic stimulation (100 Hz for 1 second). Data were acquired using the MultiClamp 700B amplifier and pClamp 10 software (Molecular Devices). Analysis of fEPSPs was performed with a Python custom program. The paired-pulse ratio was computed as the ratio between the fEPSP slope of the second stimulus and the fEPSP slope of the first stimulus. LTP was calculated in a 15-minute-long window, 45 minutes after the stimulus delivery. Statistical analysis was performed using GraphPad Prism. Two-way ANOVA followed by Bonferroni's post hoc test and Student's *t* test were used to calculate statistical significance.

### Statistics

For each experiment, data were analyzed with proper statistical tools. Two-way ANOVA followed by post hoc comparisons was used. Data were also analyzed by unpaired Student's *t* test (2 tailed; CI, 95%) using GraphPad Prism statistical software. Data are expressed as mean + SEM. All results are described throughout the text by reporting for each data set the relevant statistics that were used.  $P < 0.05$  was considered significant.

### Study approval

All animal experiments were carried out in the United Kingdom under guidance issued by the Medical Research Council in *Responsibility in the Use of Animals for Medical Research* (July 1993) and Home Office project license no. 30/2198 and in Italy under project licence 106/2009 – B. All experiments conformed to international guidelines on the ethical use of animals. For human studies, written informed consent was received from legal representatives of all participants prior to inclusion. The study was approved by the local ethical committee (NL 13636.091.07).



**Acknowledgments**

We thank J. Assad, T. Fellin, F. Benfenati, F. Szele, A. Greenfield, and S. Brown for critical reading of the manuscript. We thank A. Galbusera for animal preparation and MR image acquisition. We would like to thank all patients and their relatives for their participation in these studies and Willemijn Wissink-Lindhout, Saskia van der Velde-Visser, Gaby van de Ven-Schobers, and Marga Schepens for their technical assistance. The work was supported by the Medical Research Council (United Kingdom) (to P.M. Nolan), the Istituto Italiano di Tecnologia (Italy) (to V. Tucci), and grants from the Consortium “Stronger on your own feet” (to T. Kleefstra and M.H. Willemsen), the Netherlands Organization for Health Research and Development (ZonMw) (907-00-365 to T. Kleefstra), the European Union under the 7th framework program (Gencodys

HEALTH-F4-2010-241995 to A. Vulto-vab Silfhout, Z. Iqbal, and T. Kleefstra), and the Higher Education Commission, Islamabad, Pakistan (to Z. Iqbal).

Received for publication April 8, 2013, and accepted in revised form January 9, 2014.

Address correspondence to: Valter Tucci, Istituto Italiano di Tecnologia, Neuroscience and Brain Technologies, Via Morego, 30, Genova, 16163, Italy. Phone: 3901071781; Fax: 3901071781230; E-mail: valter.tucci@iit.it. Or to: Patrick M. Nolan, MRC Harwell, Harwell Science and Innovation Campus, Oxfordshire, OX11 0RD, United Kingdom. Phone: 441235841200; Fax: 441235841200; E-mail: p.nolan@har.mrc.ac.uk.

1. Jamieson C, Sharma M, Henderson BR. Wnt signaling from membrane to nucleus:  $\beta$ -catenin caught in a loop. *Int J Biochem Cell Biol.* 2012;44(6):847–850.
2. Xing Y, et al. Crystal structure of a full-length  $\beta$ -catenin. *Structure.* 2008;16(3):478–487.
3. Grigoryan T, Wend P, Klaus A, Birchmeier W. Deciphering the function of canonical Wnt signals in development and disease: conditional loss- and gain-of-function mutations of  $\beta$ -catenin in mice. *Genes Dev.* 2008;22(17):2308–2341.
4. Salinas PC, Price SR. Cadherins and catenins in synapse development. *Curr Opin Neurobiol.* 2005; 15(1):73–80.
5. Huber AH, Weis WI. The structure of the  $\beta$ -catenin/E-cadherin complex and the molecular basis of diverse ligand recognition by  $\beta$ -catenin. *Cell.* 2001;105(3):391–402.
6. Muller T, Choidas A, Reichmann E, Ullrich A. Phosphorylation and free pool of  $\beta$ -catenin are regulated by tyrosine kinases and tyrosine phosphatases during epithelial cell migration. *J Biol Chem.* 1999;274(15):10173–10183.
7. Pathre P, et al. PTP1B regulates neurite extension mediated by cell-cell and cell-matrix adhesion molecules. *J Neurosci Res.* 2001;63(2):143–150.
8. Murase S, Mosser E, Schuman EM. Depolarization drives  $\beta$ -catenin into neuronal spines promoting changes in synaptic structure and function. *Neuron.* 2002;35(1):91–105.
9. Kandel ER. The molecular biology of memory storage: a dialogue between genes and synapses. *Science.* 2001;294(5544):1030–1038.
10. Maguschak KA, Ressler KJ.  $\beta$ -Catenin is required for memory consolidation. *Nat Neurosci.* 2008; 11(11):1319–1326.
11. O’Roak BJ, et al. Multiplex targeted sequencing identifies recurrently mutated genes in autism spectrum disorders. *Science.* 2012;338(6114):1619–1622.
12. O’Roak BJ, et al. Sporadic autism exomes reveal a highly interconnected protein network of de novo mutations. *Nature.* 2012;485(7397):246–250.
13. de Ligt J, et al. Diagnostic exome sequencing in persons with severe intellectual disability. *N Engl J Med.* 2012;367(20):1921–1929.
14. Nolan PM, et al. A systematic, genome-wide, phenotype-driven mutagenesis programme for gene function studies in the mouse. *Nat Genet.* 2000; 25(4):440–443.
15. Fossat N, et al. Stringent requirement of a proper level of canonical WNT signalling activity for head formation in mouse embryo. *Development.* 2011; 138(4):667–676.
16. Lilien J, Balsamo J. The regulation of cadherin-mediated adhesion by tyrosine phosphorylation/dephosphorylation of  $\beta$ -catenin. *Curr Opin Cell Biol.* 2005;17(5):459–465.
17. Xu W, Kimelman D. Mechanistic insights from structural studies of  $\beta$ -catenin and its binding partners. *J Cell Sci.* 2007;120(pt 19):3337–3344.
18. Chenn A, Walsh CA. Regulation of cerebral cortical size by control of cell cycle exit in neural precursors. *Science.* 2002;297(5580):365–369.
19. Mandillo S, et al. Reliability, robustness, and reproducibility in mouse behavioral phenotyping: a cross-laboratory study. *Physiol Genomics.* 2008; 34(3):243–255.
20. Morris R. Developments of a water-maze procedure for studying spatial learning in the rat. *J Neurosci Methods.* 1984;11(1):47–60.
21. Johansen JP, Cain CK, Ostroff LE, LeDoux JE. Molecular mechanisms of fear learning and memory. *Cell.* 2011;147(3):509–524.
22. Gallistel CR, King A, McDonald R. Sources of variability and systematic error in mouse timing behavior. *J Exp Psychol Anim Behav Process.* 2004;30(1):3–16.
23. Lassi G, et al. Loss of Gnas imprinting differentially affects REM/NREM sleep and cognition in mice. *PLoS Genet.* 2012;8(5):e1002706.
24. Balci F, Freestone D, Gallistel CR. Risk assessment in man and mouse. *Proc Natl Acad Sci U S A.* 2009; 106(7):2459–2463.
25. O’Roak BJ, et al. Multiplex targeted sequencing identifies recurrently mutated genes in autism spectrum disorders. *Science.* 2012;338(6114):1619–1622.
26. Cao F, et al. Alteration of astrocytes and Wnt/ $\beta$ -catenin signaling in the frontal cortex of autistic subjects. *J Neuroinflammation.* 2012;9(1):223.
27. Campos VE, Du M, Li Y. Increased seizure susceptibility and cortical malformation in  $\beta$ -catenin mutant mice. *Biochem Biophys Res Commun.* 2004; 320(2):606–614.
28. Machon O, van den Bout CJ, Backman M, Kemler R, Krauss S. Role of  $\beta$ -catenin in the developing cortical and hippocampal neuroepithelium. *Neuroscience.* 2003;122(1):129–143.
29. Schüller U, Rowitch DH.  $\beta$ -Catenin function is required for cerebellar morphogenesis. *Brain Res.* 2007;1140:161–169.
30. Huelsken J, Vogel R, Brinkmann V, Erdmann B, Birchmeier C, Birchmeier W. Requirement for  $\beta$ -catenin in anterior-posterior axis formation in mice. *J Cell Biol.* 2000;148(3):567–578.
31. van Veelen W, et al.  $\beta$ -Catenin tyrosine 654 phosphorylation increases Wnt signalling and intestinal tumorigenesis. *Gut.* 2011;60(9):1204–1212.
32. Sharma M, Jamieson C, Johnson M, Molloy MP, Henderson BR. Specific armadillo repeat sequences facilitate  $\beta$ -catenin nuclear transport in live cells via direct binding to nucleoporins Nup62, Nup153, and RanBP2/Nup358. *J Biol Chem.* 2012; 287(2):819–831.
33. Piedra J, Martinez D, Castano J, Miravet S, Dunach M, de Herrerros AG. Regulation of  $\beta$ -catenin structure and activity by tyrosine phosphorylation. *J Biol Chem.* 2001;276(23):20436–20443.
34. Yu X, Malenka RC.  $\beta$ -Catenin is critical for dendritic morphogenesis. *Nat Neurosci.* 2003; 6(11):1169–1177.
35. Buenavista MT, Roche DB, McGuffin LJ. Improvement of 3D protein models using multiple templates guided by single-template model quality assessment. *Bioinformatics.* 2012;28(14):1851–1857.
36. Roche DB, Buenavista MT, Tetchner SJ, McGuffin LJ. The IntFOLD server: an integrated web resource for protein fold recognition, 3D model quality assessment, intrinsic disorder prediction, domain prediction and ligand binding site prediction. *Nucleic Acids Res.* 2011;39(Web Server issue):W171–W176.
37. Esapa CT, et al. SGCE missense mutations that cause myoclonus-dystonia syndrome impair epsilon-sarcoglycan trafficking to the plasma membrane: modulation by ubiquitination and torsinA. *Hum Mol Genet.* 2007;16(3):327–342.
38. Avants BB, Epstein CL, Grossman M, Gee JC. Symmetric diffeomorphic image registration with cross-correlation: evaluating automated labeling of elderly and neurodegenerative brain. *Med Image Anal.* 2008;12(1):26–41.
39. Scattoni ML, Crawley J, Ricceri L. Ultrasonic vocalizations: a tool for behavioural phenotyping of mouse models of neurodevelopmental disorders. *Neurosci Biobehav Rev.* 2009;33(4):508–515.
40. Tucci V, Hardy A, Nolan PM. A comparison of physiological and behavioural parameters in C57BL/6j mice undergoing food or water restriction regimes. *Behav Brain Res.* 2006;173(1):22–29.
41. Giacomini C, et al. Both Schwann cell and axonal defects cause motor peripheral neuropathy in Ebf2<sup>-/-</sup> mice. *Neurobiol Dis.* 2011;42(1):73–84.
42. Vandesompele J, et al. Accurate normalization of real-time quantitative RT-PCR data by geometric averaging of multiple internal control genes. *Genome Biol.* 2002;3(7):RESEARCH0034.
43. Berdondini L, et al. Active pixel sensor array for high spatio-temporal resolution electrophysiological recordings from single cell to large scale neuronal networks. *Lab On A Chip.* 2009;9(18):2644–2651.
44. Imfeld K, et al. Large-scale, high-resolution data acquisition system for extracellular recording of electrophysiological activity. *IEEE Trans Biomed Eng.* 2008;55(8):2064–2073.
45. Maccione A, Gandolfo M, Massobrio P, Novellino A, Martinoia S, Chiappalone M. A novel algorithm for precise identification of spikes in extracellularly recorded neuronal signals. *J Neurosci Methods.* 2009; 177(1):241–249.
46. Chiappalone M, Novellino A, Vajda I, Vato A, Martinoia S, van Pelt J. Burst detection algorithms for the analysis of spatio-temporal patterns in cortical networks of neurons. *Neurocomputing.* 2005; 65–66:653–662.